

Studying the formation and neutralization of an ion thruster plume with EP2PLUS

IEPC-2019-491

*Presented at the 36th International Electric Propulsion Conference
University of Vienna, Austria
September 15-20, 2019*

Jesús Perales ^{*}, Filippo Cichocki [†], Mario Merino [‡] and Eduardo Ahedo [§]
Equipo de propulsión espacial y plasmas (EP2), Universidad Carlos III de Madrid, Leganés, Spain

A 3D hybrid particle-in-cell/fluid model is presented and applied to the simulation of an ion thruster grid optics, to study both the charge and electric current neutralization in the near plume. While a non-linear Poisson solver is used to obtain the electric potential, assuming a Boltzmann relation for the electron density, the electric continuity and electron momentum equation are solved together through a thermalized potential function, whose gradient permits to compute the electric and electron current density. Both a symmetric single-aperture and a multi-aperture problem are analysed and the obtained plasma plume properties are compared along the thruster centerline beamlet. It is found that the effects of the center beamlet interaction with the others can be successfully modeled through a specular macro-particles reflection at the lateral boundaries of the single-aperture simulation domain. Moreover, both single and multi-apertures simulations show that the charge and current neutralization generally occur at different distances from the acceleration grid. While the charge neutralization is independent of the neutralizer position, the electric current neutralization is strongly affected by it, and can thus present important asymmetries.

Nomenclature

Φ	= thermalized potential
ϕ	= electric potential
\mathbf{E}	= electric field vector
e	= elementary electron charge
m_e	= elementary electron mass
m_s	= elementary mass of the s^{th} heavy particle species population
h_e	= electron barotropy function
n_e	= electron number density
n_s	= number density of s^{th} heavy particle species population
p_e	= electron pressure
T_e	= electron temperature
σ_e	= electron scalar conductivity
P	= perveance
NPH	= normalized perveance per hole
I_b	= beam current
V_T	= total extraction voltage

*Master student, jperales@ing.uc3m.es.

†Assistant professor, Aerospace Engineering department, fcichock@ing.uc3m.es.

‡Associate professor, Aerospace Engineering department, mario.merino@uc3m.es

§Professor, Aerospace Engineering department, eduardo.ahedo@uc3m.es

V_S	= voltage drop between source plasma and screen grid
V_n	= effective acceleration voltage
R	= net-to-total acceleration voltage ratio
α	= beam divergence angle
ν_{es}	= electron momentum transfer frequency with the s^{th} heavy particle population
ν_e	= total electron momentum transfer collision frequency
Z_s	= charge number of the s^{th} heavy particle species population
\mathbf{u}_e	= electron fluid velocity
\mathbf{u}_s	= fluid velocity of the s^{th} heavy particle species population
\mathbf{g}_e	= electron flux vector
\mathbf{g}_s	= flux vector of the s^{th} heavy particle species population
\mathbf{j}_i	= total ion current density vector
\mathbf{j}_e	= electron current density vector
\mathbf{j}_c	= collisional current density vector
\mathbf{r}_j	= individual position vector of the j^{th} macro-particle
\mathbf{v}_j	= individual velocity vector of the j^{th} macro-particle
Δt	= PIC time step for advancing macro-particles
d_s	= screen grid hole side
d_a	= acceleration grid hole side
l_g	= grids gap
t_s	= screen grid thickness
t_a	= acceleration grid thickness
l_e	= effective acceleration length

I. Introduction

The ion optics is the device in charge of extracting, accelerating and focusing a beam of charged particles. The three mentioned processes significantly impact the performance and lifetime of any thruster based on the use of such a device. Hence, since the early age of space propulsion, the ion optics problem has drawn a great attention in the scientific community. Since then, already flying thrusters experience¹ and *ad hoc* experimental studies² have permitted to increase the knowledge on the field and, as a consequence, to improve the design of the device. Nevertheless, the inherent limitations of the experimental research, basically the time and monetary cost, have fostered the study of ion optics performance through computer simulations, with everyday more and more complex models, featuring Particle-in-Cell (PIC) solvers.

These computer simulations must be able to faithfully reproduce the main quality parameters of any ion optics device, namely: perveance, beam divergence angle, beam flatness, electron backstreaming voltage. The first two will be dealt with in the present work. The perveance is mathematically defined as:

$$P = \frac{I_b}{V_T^{3/2}}, \quad (1)$$

where I_b is the ion current carried by the beam and V_T is the electric potential difference between the discharge chamber plasma and the acceleration grid, as shown in Fig. 1. The perveance serves to quantify the relative influence on the electric field of the space charge compared to that of the grid assembly. A relatively large value of this metric leads to an underfocused beam, while a small value implies overfocusing. In this work, instead of the perveance P , we shall use the Normalized Perveance per Hole (*NPH*), defined as:

$$NPH = \frac{I_b}{V_T^{3/2}} \left(\frac{l_e}{d_s} \right)^2 \quad (2)$$

where l_e is the effective acceleration length

$$l_e = \left(l_g^2 + \frac{d_s^2}{4} \right)^{1/2}, \quad (3)$$

where l_g and d_s are respectively the axial distance between the grids (or grid gap) and the size of a screen grid hole.

Apart from the perveance and these geometric parameters, another important parameter influencing the beam focusing is the net acceleration voltage, V_n , which is defined in Fig. 1.

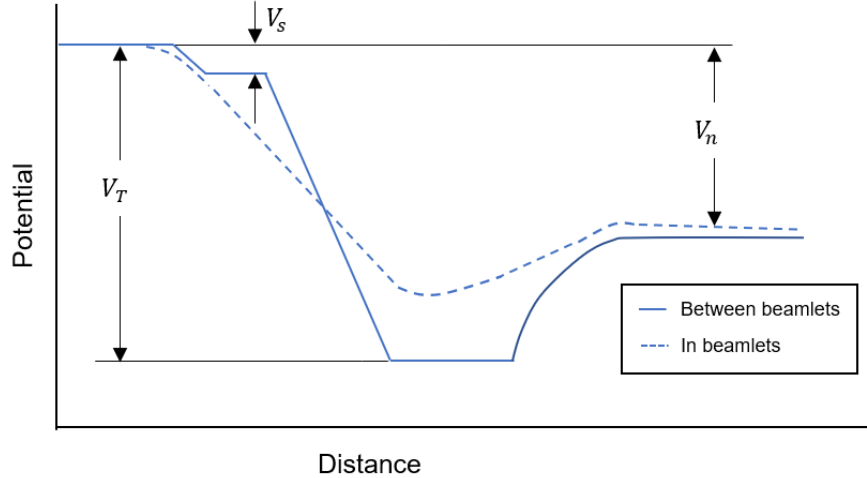


Figure 1: Potential evolution.

A good estimate of how well a beam is focused is then provided by the divergence angle α , defined experimentally as:

$$\alpha = \arctan\left(\frac{R_{95}}{L}\right), \quad (4)$$

where R_{95} represents the radius (from the thruster centerline) of the 95% ion current streamline and L is the distance between the acceleration grid and the plane of measurement. Another possible definition that is generally adopted in simulation codes,³ is the slope angle (measured from the horizontal centerline direction) of the 95% ion current fluid streamline. The above two definitions tend to one another for increasing distances L between the acceleration grid and the measurement plane.

In order to assess all these quality parameters, many codes have been developed. There exist 3D codes⁴ as well as 2D codes,⁵ the latter taking advantage of the axial symmetry of the problem. Although some codes simulate the whole grids assembly,⁶ in general, a reduced, but significant, portion of it is modeled. Moreover, some more sophisticated codes are able to modify the geometry of the grids during the simulation run based on the simulated erosion pattern.⁷ Diverse meshing strategies have also been addressed, such as the IFE (Immersed Finite Elements) method.⁸ Finally, regarding the modeling of the electrons, they are typically treated as a fluid, yielding Hybrid fluid-PIC codes. Yet, full PIC codes are also considered,⁹ in which electrons are treated as particles, in the same way as the heavy species, at the cost of a much larger computational effort.

The code considered in this paper is a three-dimensional hybrid PIC-fluid code,^{10,11} named EP2PLUS (Extensible Parallel Plasma PLUme Simulator), which can solve both a non-linear Poisson equation to obtain the electric potential, but also the combined electric continuity and electron momentum equations, in order to obtain the electron and electric current density and streamlines. With this simulation code, we shall focus on several ion optics topics: the influence of the perveance on the divergence angle, the effect of ion beamlets coalescence, and the electric charge and current neutralization. To do so, both single and multi-apertures simulations will be carried out and their results discussed. Since a simple rectangular 3D PIC mesh is used, the grid holes will feature a simplifying square shape.

The paper is finally structured as follows. Firstly, both the PIC and the electron model are presented in Sec. II. Then the single-aperture simulations are presented and discussed in Sec. III, while the multi-aperture simulation is dealt with in Sec. IV. A comparison between single and multi-apertures simulations is carried out in Sec. V, while numerical simulations are compared with experiments in Sec. VI. Finally, conclusions and future work are summarized in Sec. VII.

II. Hybrid model

A detailed explanation of the characteristics and structure of the EP2PLUS code can be found in Refs. 10 and 11. In the following lines the main features of both the PIC and electron models will be briefly presented, focusing only on the aspects that are of particular interest for the present case of study (ion grid optics).

Regarding in first place the treatment of the heavy species, ions and neutrals, these are modeled as macro-particles by the dedicated PIC module. The macro-particles position and velocity are obtained by numerical integration of the dynamic equations by means of the so-called leap-frog scheme, and the integration time step must be sufficiently small to satisfy the Courant condition.¹²

Regarding the boundary conditions for the PIC macro-particles, and referring to Fig. 2, the following types are considered:

- **Free Loss Surface:** when a particle crosses a free-loss boundary, it is removed from the simulation. By default, the external boundaries are of this type.
- **Transparent Surface:** when a particle crosses this type of surface, it crosses it without further effects. An example of such a surface is the current neutralizer surface (which emits electrons for neutralization and is transparent to ions and neutrals), as considered in the single-aperture simulations.
- **Wall Surfaces:** when ion macro-particles collide with such surfaces they suffer a recombination with local electrons, so that neutral macro-particles are re-injected into the domain. Neutral macro-particles, on the other hand, are simply reflected. In the current work, the neutral re-emission (due to recombination) or reflection is simulated as a diffuse reflection phenomenon with a perfect thermal accommodation with the wall material.¹¹
- **Injection Surfaces:** the injection surfaces are the ones from which macro-particles are injected (of any type) following a drifting Maxwellian distribution with a given temperature, velocity and particle flux.¹¹ In this paper, only the left upstream simulation boundary is considered to be of this type, and simulates the incoming ion and neutral flux from the discharge chamber.
- **Specular Reflection Surfaces:** when crossing such surfaces, all heavy species macro-particles are specularly reflected. These surfaces permit to set symmetric boundary conditions for the macro-particles thus permitting, in the single-aperture simulations, to reproduce the interaction of the simulated beamlet with the rest of thruster beamlets (not simulated in such a case).

Unlike the heavy species, the electrons are treated as a fluid, in order to reduce the simulation computational cost, as done by the great majority of existing codes for ion optics analysis. In the present work, the electron fluid properties are obtained by solving the coupled equations of electron momentum balance, electric current continuity and Poisson equations:

$$\begin{cases} 0 = -\nabla p_e - en_e \mathbf{E} - \sum_s \nu_{es} m_e n_e (\mathbf{u}_e - \mathbf{u}_s), & (5) \\ 0 = \nabla \cdot (\mathbf{j}_e + \mathbf{j}_i), & (6) \\ \nabla^2 \phi = \frac{e(n_e - \sum_s Z_s n_s)}{\epsilon_0}, & (7) \end{cases}$$

where $\mathbf{E} = -\nabla\phi$ is the electric field, $p_e = n_e T_e$ is the scalar electron pressure, m_e is the elementary electron mass, \mathbf{u}_e and \mathbf{u}_s are respectively the fluid velocities of electrons and of the s^{th} heavy particle population, ν_{es} is the momentum transfer collision frequency between electrons and the s^{th} heavy particle population, \mathbf{j}_e and \mathbf{j}_i are the electron and total ion current densities, and Z_s is the charge number of the s^{th} heavy particle population. Note that the summation terms extend to all applicable heavy particle populations (e.g., in this case, singly-charged ions and neutrals).

In this work, in order to deal with ion optics simulations, two separate and isothermal electron populations are considered: a first one inside the discharge chamber to model the source electrons, and a second one outside of the thruster to model neutralizer electrons. Source electrons are characterized by the temperature $T_{e0}^{(1)}$, while neutralizer electrons have a temperature $T_{e0}^{(2)}$. Now we introduce the thermalized potential Φ , whose gradient is $\nabla\Phi = \nabla\phi - \nabla p_e/n_e$. If we integrate this differential relation, we obtain a Boltzmann-like expression for the electron density of both populations:

$$n_e^{(j)}(\phi, \Phi) = n_{e0}^{(j)} \exp\left(\frac{e((\phi - \phi_0^{(j)}) - (\Phi - \Phi_0^{(j)}))}{T_{e0}^{(j)}}\right), \quad (8)$$

where (j) is the electron population index ((1) or (2) in this case), and $\phi_0^{(j)}$, $\Phi_0^{(j)}$ are respectively the electric potential and thermalized potential values at the reference points of the electron populations. At such points, the electron density is assumed to be known and given by $n_e = n_{e0}^{(j)} = \sum_s Z_s n_s$, i.e. we assume quasineutrality there. Poisson equation, Eq. 7, permits to obtain both the electron density and the electric potential by solving a non-linear equation, in which the electron density is an explicit function of the electric potential, as shown in Eq. 8.

The thermalized potential Φ measures the deviation of the electric potential from its Boltzmann solution, due to collisional effects on the electrons. In particular, in this ion optics case, we have:

$$\phi - \phi_0^{(j)} = \frac{T_{e0}^{(j)}}{e} \ln\left(\frac{n_e}{n_{e0}^{(j)}}\right) + (\Phi - \Phi_0^{(j)}). \quad (9)$$

In order to obtain the thermalized potential Φ , the system formed by the electron momentum balance and electric current continuity equations has to be solved. As shown in Ref. 11, these equations can be reduced to an elliptic equation for Φ :

$$\nabla^2 \Phi + \nabla \Phi \cdot \nabla \ln(\sigma_e) = \frac{\nabla \cdot (\mathbf{j}_i - \mathbf{j}_c)}{\sigma_e}, \quad (10)$$

where $\sigma_e = e^2 n_e / (m_e \nu_e)$ is the scalar electron conductivity, $\nu_e = \sum_s \nu_{es}$ is the total electron collision momentum transfer frequency, and \mathbf{j}_c is a collisional current density defined as:

$$\mathbf{j}_c = \frac{en_e}{\nu_e} \sum_s \nu_{es} \mathbf{u}_s. \quad (11)$$

Once Φ has been computed, the electron current density can be finally retrieved as:

$$\mathbf{j}_e = -\sigma_e \nabla \Phi - \mathbf{j}_c. \quad (12)$$

Poisson equation for ϕ and Eq.10 for Φ are not solved for simultaneously at the same time step. For simplicity, and without affecting the solution of a stationary problem, the elliptic equation for Φ is solved first, using the electron density obtained in the previous time step solution (to compute σ_e and \mathbf{j}_c). Then, we solve the non-linear Poisson equation for ϕ , with the updated value of Φ . For unmagnetized simulations, as shown in the next section results, the correction $\Phi - \Phi_0^{(j)}$ is generally very small everywhere (in the order of mV), and has negligible effects on the solution of the non-linear Poisson equation, Eq. 7. This means that the electric potential is almost independent of the thermalized potential, while the opposite is not true, since the latter depends on the electron conductivity σ_e , strongly affected by n_e , and hence ϕ .

As shown in Fig. 2, the simulation domain is subdivided into two regions (the source and neutralizer electrons regions) by a vertical separation line. Given the exponential nature of Eq. 8, in order to avoid numerical instabilities during the initial simulation transient, we have decided to actively control the position of this separation line, to make it coincide at all times with that of the minimum electric potential along the beamlet centerline. This permits us to enhance the convergence of the Poisson solver during the initial transient phase, and to consistently solve for the downstream region, without the need of linearizing Eq. 8 for $\phi > \phi_0^{(j)}$, i.e. when the electric potential is higher than the downstream electrons reference potential, a trick considered by most authors in the literature to avoid numerical instabilities.

The boundary conditions for the computation of both ϕ and Φ are finally summarized in Fig. 2. Regarding the former, this is set at the two reference electron points (marked by red dots in the figure), and at the screen and acceleration grid walls. At the other boundaries, on the other hand, an homogeneous Neumann condition is applied, corresponding to a zero normal electric field. For what concerns Φ , this is set to a constant value at the neutralizer points (in the single-beamlet simulations, these correspond to a plane at a given distance downstream, while in the multi-aperture simulation, these correspond to the exit emission surface of the neutralizer). This is equivalent to leaving the electron current density free. At the other

boundaries, we impose a value for the the normal electron current density. This corresponds to a non-homogeneous Neumann condition, since it is equivalent to imposing the directional derivative of Φ along the boundary normal direction $\mathbf{1}_n$:

$$\frac{\partial \Phi}{\partial \mathbf{1}_n} = -\frac{1}{\sigma_e} (\mathbf{j}_e + \mathbf{j}_c) \cdot \mathbf{1}_n. \quad (13)$$

While at the screen and acceleration grid walls, the electron current density is equal to the thermal electron current density $j_{e,th}$, which is an explicit function of the local electron density and temperature (as obtained from Poisson equation solution), at the external boundaries, the electron current density is set to be equal in magnitude and opposite in sign to the ion current density. This corresponds to imposing locally a zero normal electric current density.

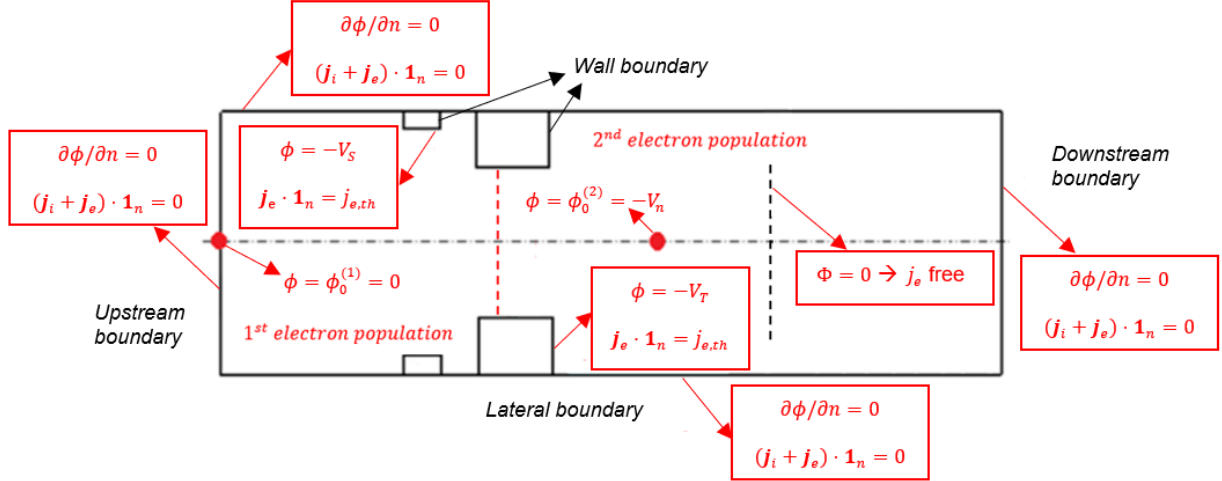


Figure 2: Boundary conditions for ϕ and Φ , and types of boundaries for the PIC macro-particles.

III. Single aperture simulations

Firstly, a set of single aperture simulations is carried out. The main simulation and geometric parameters are specified in Tab.1. Two different setups have been considered, differing only in terms of grid holes

Table 1: Simulation parameters for the single-aperture simulations. Two different setups have been considered, differing in grid holes geometry and effective acceleration voltage.

Parameters	Units	Setup 1	Setup 2
$T_{e0}^{(1)}$	eV	3.5	3.5
$T_{e0}^{(2)}$	eV	2	2
V_T	V	1100	1100
V_n	V	770	940
V_S	V	40	40
Inflow Xe ion velocity	m/s	2500	2500
Inflow Xe neutral velocity	m/s	400	400
d_s	mm	2.0	2.4
d_a	mm	1.2	1.2
l_g	mm	1.6	0.4
t_s	mm	0.4	0.4
t_a	mm	0.8	0.8

geometry and effective acceleration voltages. In all cases, in order to simulate the beamlet interactions with the surrounding ones, macro-particles are specularly reflected at the lateral boundaries of Fig. 2. Moreover, for each parameters setup, several runs are performed for different values of the perveance, by varying the plasma density inside the chamber, and hence the beam current (with constant voltage drops V_T and V_n). The reference point of the second electron population is set at the downstream boundary for setup 1 and at $z = 8$ mm for setup 2, with a reference potential of respectively -770 and -940 V. Finally, in order to simplify the analysis, no collisions are considered for the heavy species particles (neither charge-exchange nor ionization collisions).

Fig. 3 and Fig. 4 show respectively the ion density and individual trajectories in the beamlet meridional plane ($y = 0$), for three different perveance cases. As expected, the ion beamlet is more and more focused as the perveance is decreased. When the perveance is highest (Fig. 3a) the beamlet is clearly underfocused and presents very distinguished peripheral density peaks. On the contrary, when the perveance is smallest (Fig. 3c), the beamlet becomes overfocused, and individual ion trajectories cross each other, as clearly shown in Fig. 4c. In principle, in Fig. 3b, we observe an intermediate case, in which the divergence angle of the beamlet is smaller than in the other two cases, and, in fact, Fig. 4b confirms that individual ion trajectories never cross each other (even downstream).

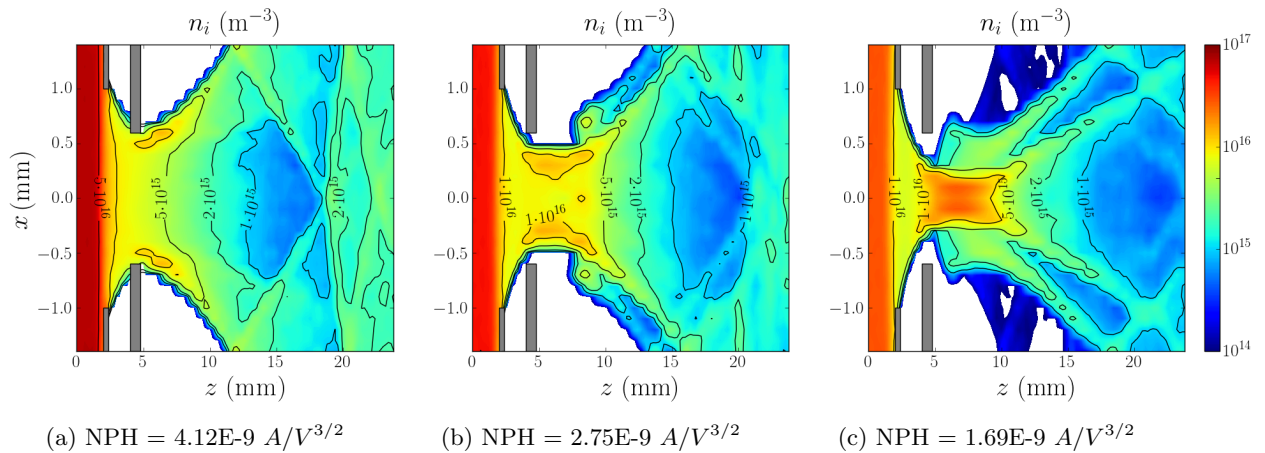


Figure 3: Ion density contour plots at $y = 0$, for a varying perveance, for the setup N. 1 of Tab. 1.

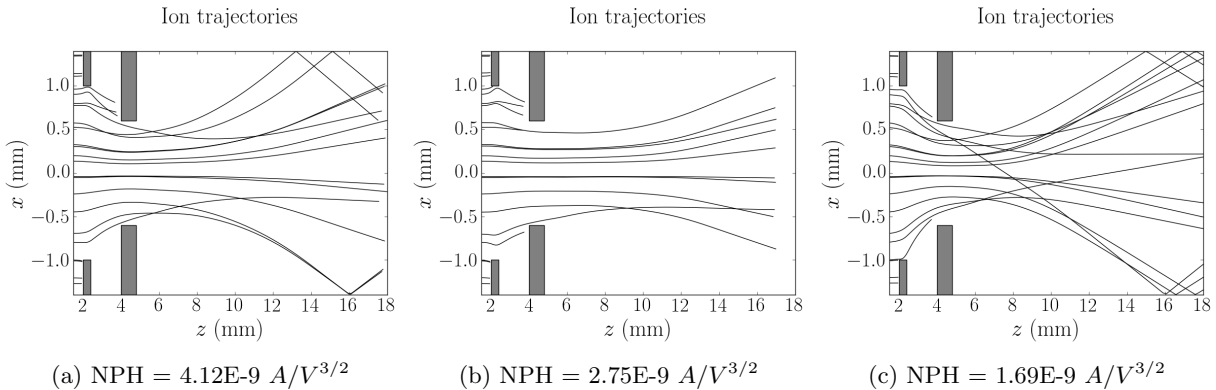


Figure 4: Trajectories of ion macroparticles for a varying perveance, for the setup N. 1 of Tab. 1.

The fact that Fig. 3b represents an intermediate case can be checked by means of the beamlet divergence angle evolution, as shown by the blue solid line of Fig. 15. Clearly, we can observe the existence of an optimal perveance, for which the divergence angle is minimum, and we observe that the case in Fig. 3b is close to this optimal value and, therefore, is an intermediate case.

An ion beam is overfocused, underfocused or well-focused depending on the shape of the extraction

plasma sheath forming at the screen grid holes. For this reason, the detailed shape of this sheath, for each of the previous perveance cases, is displayed in Figs. 5, in terms of the charge density, and for Setup N.2.

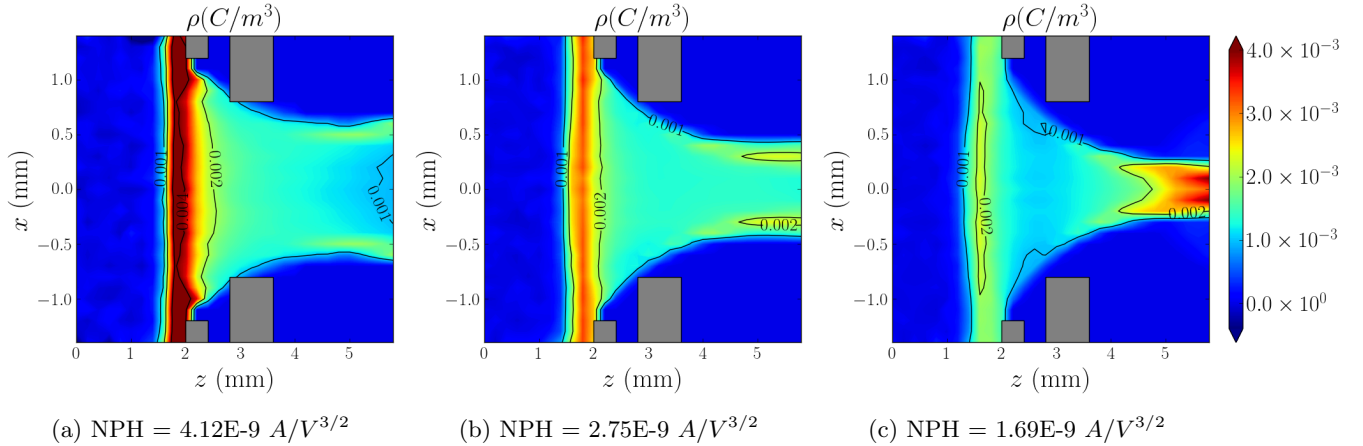


Figure 5: Charge density contour plots at $y = 0$ for a varying perveance, for the setup N. 2 of Tab. 1.

In the largest perveance case (Fig. 5a) the ion space charge dominance over the electric field “pushes” the sheath towards the inter-grid region, making it flat, or even slightly curved outwards. This shape is clearly not adequate for a good focusing of the ion stream, and thus, we obtain the underfocused beamlet observed before in Fig. 3a. On the contrary, in Fig. 5c, the relatively small perveance leads to a sheath excessively curved towards the ionization chamber. We know that the curvature is excessive because of the poor focusing observed in Fig. 3c. Finally, the sheath observed in Fig. 5b, slightly curved towards the chamber, appears to be adequate for a good focusing of the ions.

The results of the electric current neutralization study are now presented for the second simulation setup (see Tab.1), featuring a slight modification of the screen grid hole diameter and an important reduction of the inter-grid distance (now $l_g = 0.4$ mm). For the solution of electric currents, an emission surface or neutralizer surface perpendicular to the hole axis is considered (where $\Phi = 0$) at an axial distance of 8 mm from the source initial plane. The reference point for the downstream electron population is placed at the center of this neutralizer surface, and its electric potential fixed to the cathode electric potential (-940 V for setup N. 2 simulations). The thermalized potential Φ , still at $y = 0$, is shown in Fig. 6.

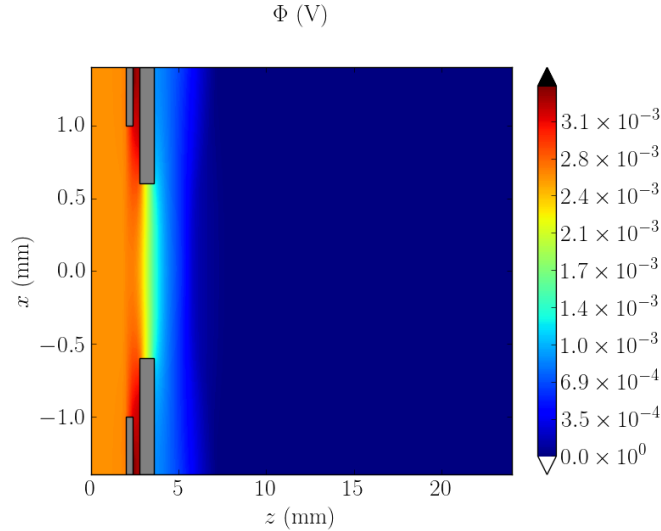


Figure 6: Thermalized potential at $y = 0$, for setup N.2 of Tab.1 with $NPH = 2.75E - 9 A/V^{3/2}$. The neutralizer plane is located at $z = 8$ mm.

By observing the absolute value of the thermalized potential, it is interesting to see that its variations are, everywhere in the domain, very small compared to those of the electric potential (mV versus kV), and therefore, although appearing in the electron density equation, Eq. 8, its influence is clearly negligible in Poisson equation. Yet, Φ and its spatial shape determine utterly the electric and electron current density.

The electron current density and the corresponding streamlines are shown in Fig. 7. The largest values are found in two clearly differentiated regions: one upstream of the screen grid, and one after the neutralizer emitting surface. In between those regions, the electron current density is relatively small, meaning that electrons are barely reaching the inter-grid region. This is found despite the large gradients of the thermalized potential between the grids and very close to the acceleration grid (see Fig. 6) because the electron conductivity σ_e and density both go to zero in such regions, due to the repelling action of the grid potentials (refer to Eq. 12 for the expression of the electron current density).

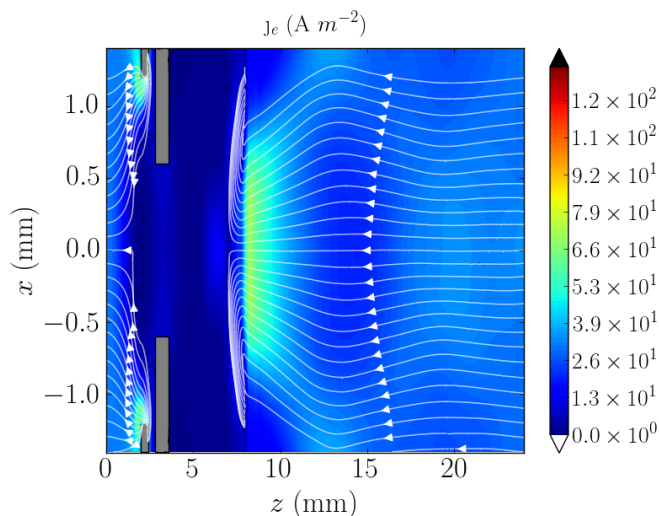


Figure 7: Electron current density at $y = 0$ with streamlines (parallel to the \mathbf{j}_e vector, and hence anti-parallel to the electron fluid velocity). Results refer to setup N.2 of Tab. 1 with $NPH = 2.75E-9 \text{ A/V}^{3/2}$. The neutralizer plane is located at $z = 8 \text{ mm}$.

Fig. 7 also shows that the electron current leaving the domain at the source plane ($z = 0$) actually comes from the screen grid (source electrons, equivalently, are collected by the screen grid). Therefore, the necessary electron current to neutralize the ion beam is injected through the neutralizer emission surface downstream, as expected. Another interesting phenomenon is that emitted neutralizer electrons first travel upstream (to neutralize the space charge of the ion beam upstream), and then they finally flow downstream to neutralize the ion current. This is consistent with what is observed by comparing the charge density and the electric current density, shown in Figs. 8a and 8b, respectively. The beamlet is already charge free at around $z = 6 \text{ mm}$ at the centerline, while it becomes current free at $z = 8 \text{ mm}$, i.e. at the axial position of the surface neutralizer. This anticipated charge neutralization is achieved by those neutralizer electrons that travel upstream after being emitted.

Still referring to Fig. 8b, right after the neutralizer emission surface, the electric current of the beam becomes practically null. The electric current streamlines clearly show that the electric current originates at the screen grid due to source electrons, it is transported through the grids by the beam ions, and it is finally absorbed by the neutralizer (where streamlines disappear). This is consistent with the physics of GITs. In fact, electrons are first collected by the screen grid, and then, through an external circuit, they are transported towards the neutralizer, where they are finally re-emitted to neutralize the ion current. The large power consumed by the power supply to transfer electrons from the high voltage screen grid to the neutralizer generally represents a large fraction of the total thruster operating power, and is known as beam power.

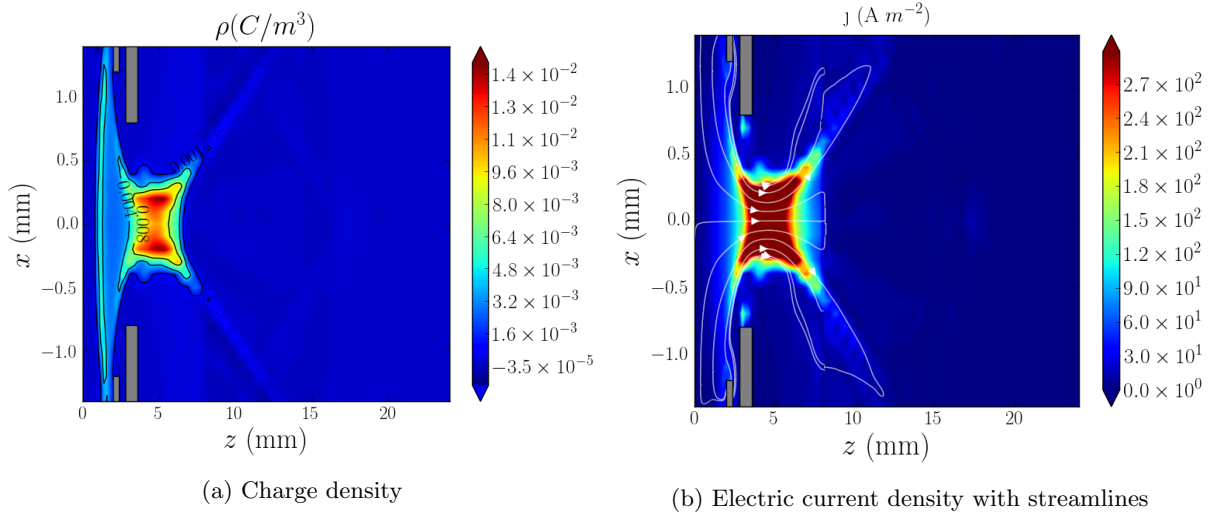


Figure 8: Charge density and electric current density at $y = 0$. Results refer to setup N. 2 of Tab.1 with $NPH = 2.75E-9 A/V^{3/2}$. The neutralizer plane is located at $z = 8$ mm.

IV. Multi-apertures simulation

Next, a simulation with a total of 9 apertures has been carried out. The main simulation parameter are again summarized in Tab. 2. It must be pointed out that, in this case, the lateral boundaries are no more specular reflection surfaces, but simply free loss surfaces. At the same time, a hollow cathode is included in the upper part of the domain, right after the acceleration grid. The internal walls upstream of the screen grid are finally assumed to be equipotential with it.

Table 2: Simulation parameters for the multi-apertures simulation. Two different setups have been considered, differing in grid holes geometry and effective acceleration voltage.

Parameters	Units	Setup 1	Setup 2
$T_e^{(1)}$	eV	3.5	3.5
$T_e^{(2)}$	eV	2.0	2.0
V_T	V	1100	1100
V_n	V	770	770
V_S	V	40	40
Inflow Xe ion velocity	m/s	2500	2500
Inflow Xe neutral velocity	m/s	400	400
Total number of apertures	(-)	9	9
d_s	mm	2.0	2.4
d_a	mm	1.2	1.2
l_g	mm	1.6	0.4
t_s	mm	0.4	0.4
t_a	mm	0.8	0.8
Neutralizer position vector (x, y, z)	mm	(5.8, 0, 5.2)	(5.8, 0, 5.2)

The domain has been sufficiently enlarged to be able to see the coalescence of the beamlets. Once again, the reference point for the second electron population is placed at the center of the emitter cathode surface, where $\phi = -V_n$, while the thermalized potential $\Phi = 0$ at all the nodes of the cathode emission surface (to leave the emitted current free).

The ion density contour at the thruster symmetry plane $y = 0$ is displayed in Fig. 9. The coalescence of the beamlets is visible and we can see clearly how the individual beamlets start to interact with each other at an axial distance of around 14 mm. Yet, at this distance, the beam properties are still not single-peaked at the centerline: only at $z \simeq 23$ mm, a center density peak appears for the first time.

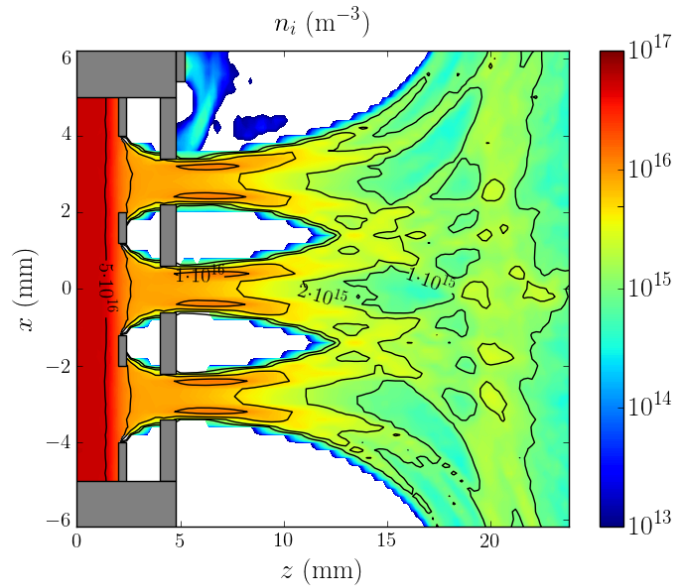


Figure 9: Ion density at $y = 0$ for the setup N.1 of Tab. 2 with $NPH = 2.75E-9 \text{ A/V}^{3/2}$.

In order to better visualize the beamlets coalescence, the ion-density is plotted in transversal planes at different axial distances from the origin. At 14 mm axial distance, right before the coalescence, we observe the structure of each individual beamlet. Interestingly the shape of the beamlets is circular, regardless of the fact that the grid holes have a square shape. At a distance of 18 mm, the beamlets have already coalesced. However, as observed in Fig. 9, there exist sharp changes on the ion density which are the reminders of the previous beamlets structures. Thus, the mixing has not been completed yet. Finally, at a distance of 24 mm, we can say that the beamlets are close to have formed a single beam: the ion density gradients are now much smoother and a density peak is emerging at the center. Nevertheless, the mixing is not complete and a faint cross-shaped ion density profile is found at this distance, which is due to the holes distribution layout on both grids.

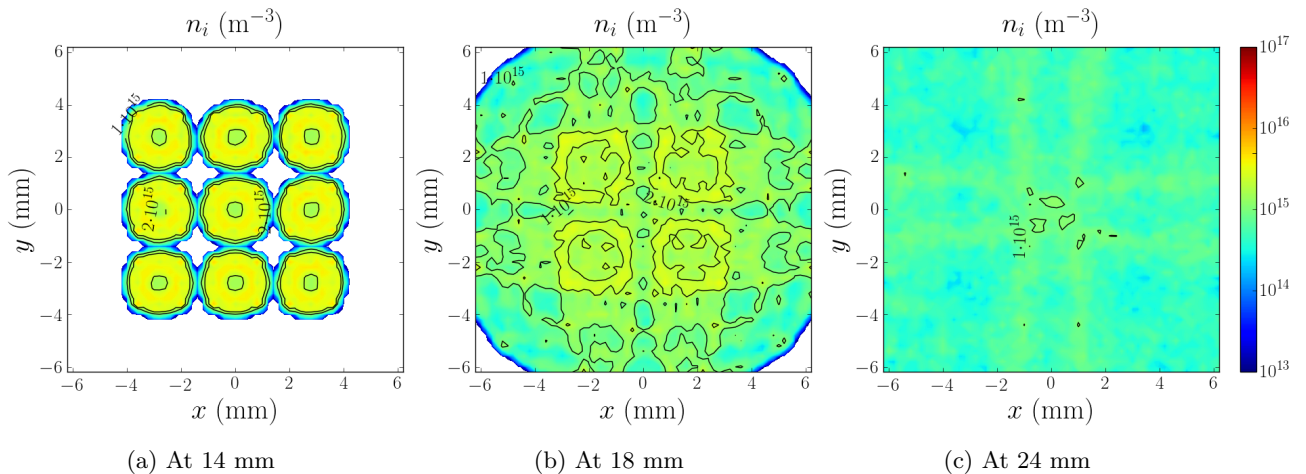


Figure 10: Ion density at different cross-sections for the setup N.1 of Tab. 2 with $NPH = 2.75E-9 \text{ A/V}^{3/2}$.

Fig. 11a then shows the charge density at $y = 0$ for the second geometry case of Tab. 2: each beamlet is neutralized at the same distance from the acceleration grid, so that the influence of the neutralizer is negligible in terms of charge neutralization. The same is not true for the electric current density, shown in Fig. 11b: each beamlet is current neutralized at a different section, depending on its distance from the neutralizer. In particular, the closer to the neutralizer, the sooner the beamlet is current-neutralized. This different behavior is the consequence of the different nature of current and charge. On one hand, the charge neutralization only depends on the local ion and electron densities, which are not affected in principle by the cathode position, but only by the local electric potential. On the other hand, the current neutralization is not only affected by the local density, but also by the ion and electron velocities; and the local velocity of the latter is certainly affected by the cathode position, both in module and direction, as shown by the streamlines of Fig. 11b. Indeed, electrons neutralizing the closest beamlets (to the cathode) follow very different trajectories from those described by electrons neutralizing the farthest beamlets.

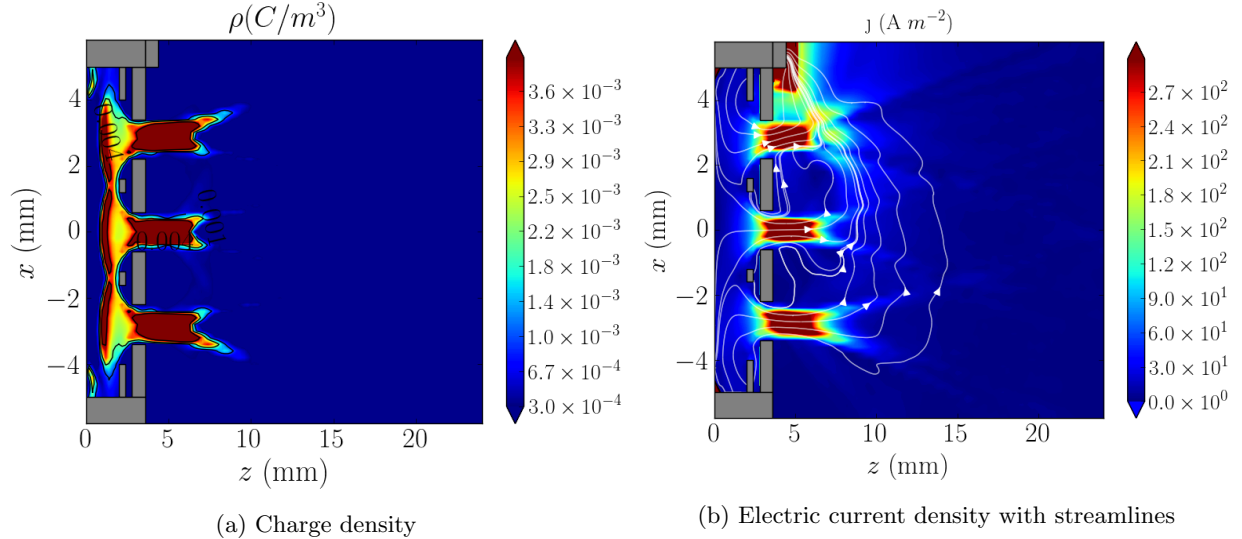


Figure 11: Charge density and electric current density at $y = 0$, for the setup N.2 of Tab. 2 with $NPH = 2.75E-9 A/V^{3/2}$.

Still regarding the electric current density, we can observe, as in the single aperture simulation, that the electric current originates at the interior of the ionization chamber, and on the walls of the chamber and of the screen grid. Then, this current travels through the grids transported by the beam ions, and is finally absorbed by the hollow cathode. As already mentioned, this electric circuit is closed by an external circuit segment that has not been shown here: the electrons collected by the screen grid and the chamber are pumped towards the cathode through an electrical connection with a beam power supply (which provides the necessary power).

Fig. 12 finally shows the electron current density and streamlines. Similarly to the single-aperture case, some electrons appear to be traveling upstream from the cathode emission surface, thus neutralizing the ion beamlets charge without neutralizing their current. In any case, all the electrons emitted by the cathode are shown to end up travelling downstream to neutralize the beam electric current.

V. Comparison of single and multi-apertures simulations

In this section, a comparison between the results of the single and the multi-apertures simulation is carried out. For this purpose, the same NPH and geometric configuration are considered for both simulations. For consistency, the single-aperture results are compared with those of the central hole of the multi-apertures case, given its symmetric position. Fig. 13 shows the comparison of ion density and electric potential along the beamlet centerline.

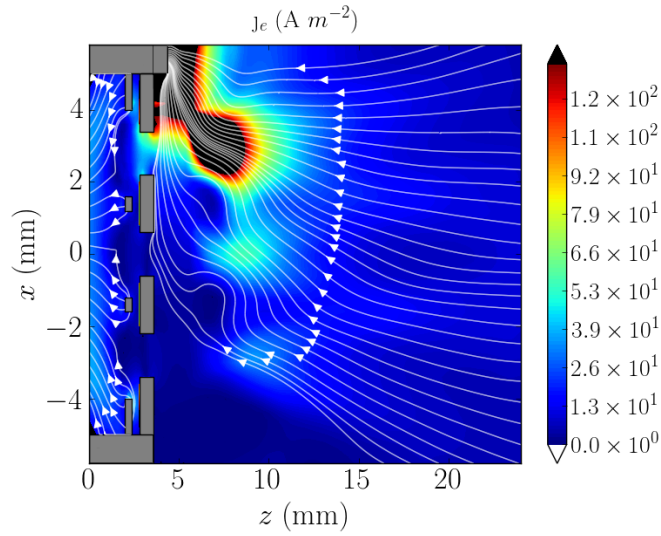


Figure 12: Electron current density at $y = 0$, for the setup N.2 of Tab. 2 with $NPH = 2.75E-9 \text{ A/V}^{3/2}$.

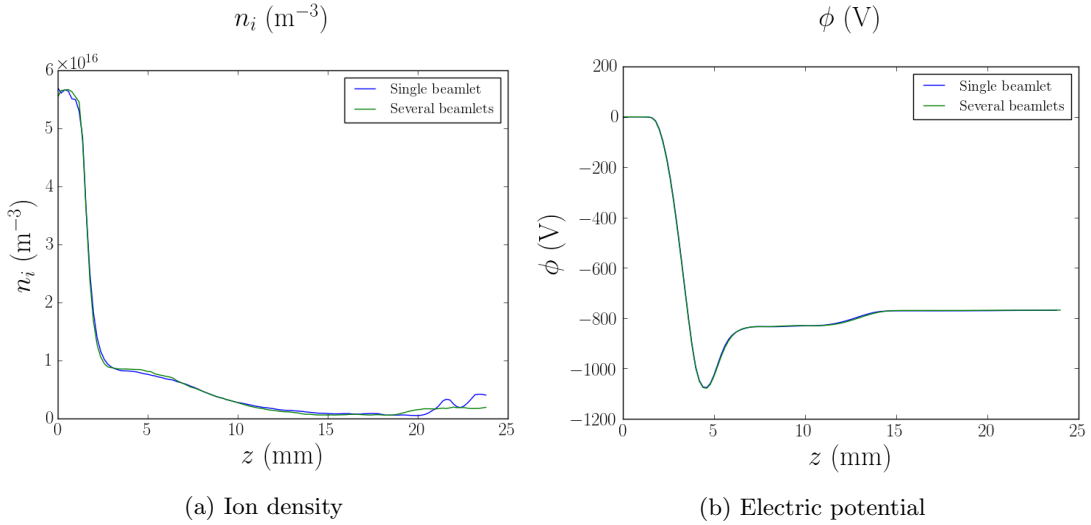


Figure 13: 1D profiles of ion density and electric potential along the axis. The shown profiles refer to the setups N.1 of Tabs. 1 and 2, with $NPH = 2.75E-9 \text{ A/V}^{3/2}$.

A good agreement is found, with both curves fitting very well. A small disagreement is observed for the ion density close to the downstream boundary, already after the beamlets coalescence. This might be due to the fact that the external beamlets which merge with the central one do not do it symmetrically, as modeled in the single aperture case, and possibly due to the influence of the neutralizer. It seems reasonable to expect that this difference would decrease with the number of simulated holes of the multi-apertures case, since the symmetry condition implicitly assume an infinite number of holes. Fig. 14 finally compares the 2D ion density maps at the meridional plane of the central beamlet.

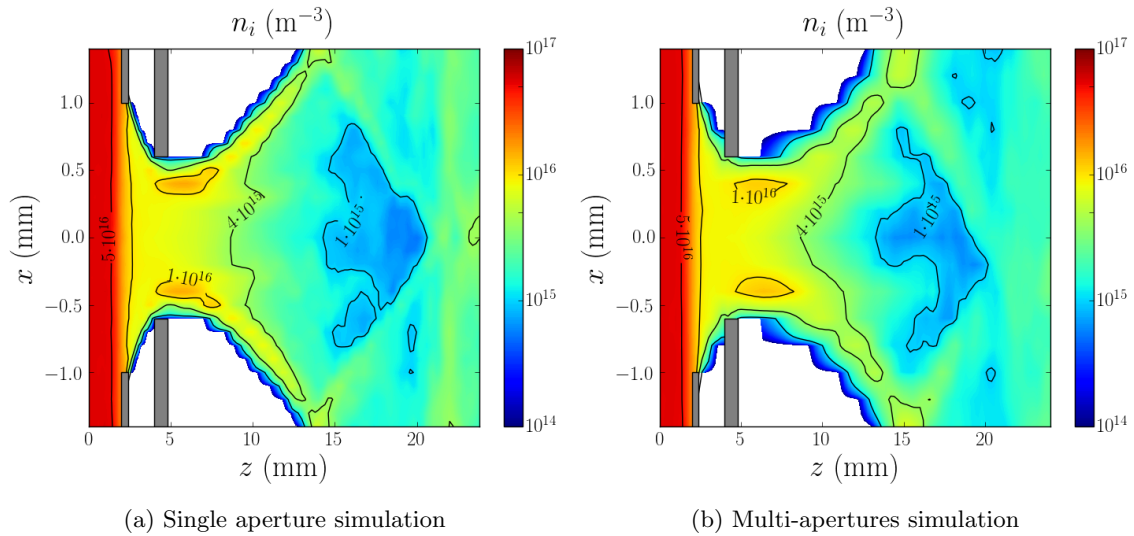


Figure 14: Ion density comparison between single and multi-apertures simulations. The central beamlet is shown for the multi-apertures case. The shown profiles refer to the setups N.1 of Tabs. 1 and 2, with $NPH = 2.75E-9 \text{ A/V}^{3/2}$.

VI. Comparison with experimental data

Finally, a comparison between the results of the numerical simulations and some experimental results reported in Ref. 2 is shown in Fig. 15, in terms of the divergence angle. The experimental results consist of several measurements of the divergence angle of the beam of an ion thruster, with a fixed geometric setup and constant V_T , V_n and V_S . The perveance is varied by acting on the ion beam current.

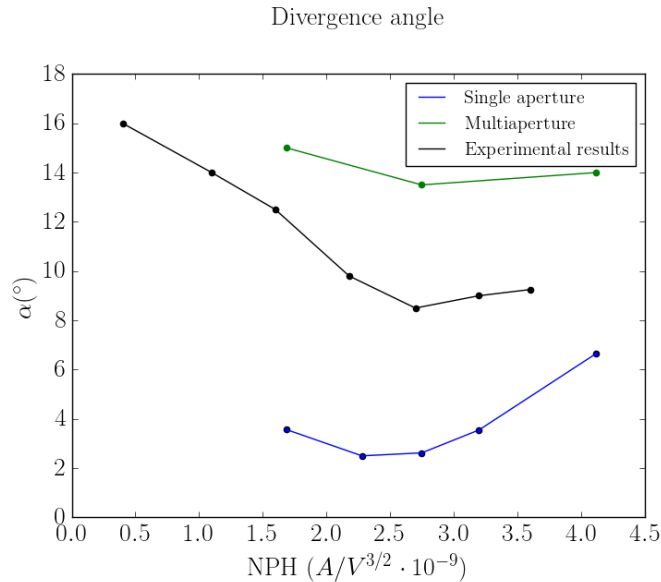


Figure 15: Evolution of the divergence angle for the single and multi-apertures simulations and from experiments,² for a varying perveance. The first simulation setup of Tabs. 1 and 2 is considered here for simulations.

Comparing the single beamlet simulation to the experiments, we notice that the angles resulting from the simulations are much smaller. This is expected given that, in these simulations, the divergence angle

is calculated for a single beamlet, not for the whole beam, prior to the beamlets coalescence. In any case, a very interesting conclusion can be drawn: the minimum point of both curves corresponds to roughly the same value of NPH . This result is of great importance, since it indicates that it is possible to use EP2PLUS single beamlets simulation for the design of actual ion thrusters, determining at which perveance regime the thruster should work.

The comparison with the multi-apertures simulation indicates, on the other hand, that our estimation of the angle is not yet as precise as it should. There are several possible explanations of this: firstly, the number of simulated holes is not realistic and such a limited number might have the effect of making peripheral border effects much larger than in reality (thus making the divergence higher). Secondly, the considered PIC mesh might not be fine enough, since small variations of the current might lead to important changes of the computed divergence angle. Finally, there are some differences between the considered geometry in the simulations and in the experiments, mainly due to meshing limitations. Nevertheless, despite the observed differences, the same optimal perveance as in the experiments can be deduced from the multi-apertures simulations.

VII. Conclusions

In this work, the EP2PLUS hybrid PIC-fluid model has been adapted to the simulation context of an ion thruster grid optics. In what regards the PIC model, a symmetric reflection boundary condition for ions and neutrals has been considered in single-aperture simulations in order to take into account the symmetric interaction of the beamlet with the surrounding ones (in a real thruster, featuring hundreds of apertures). Regarding the electron fluid model, apart from solving the non-linear Poisson equation with two reference electron populations, it permits to obtain also the electron current density and streamlines, thus enabling the study of the electric current neutralization in the near-plume, a topic that has never been addressed in the literature (at least with hybrid codes).

Several ion optics cases have been presented. Firstly, a perveance study has been carried out for a single-aperture problem. The divergence angle and other plasma features have shown the expected theoretical and experimental behavior: an optimal perveance has been found to optimize the beam focusing thus minimizing the beamlet divergence. Secondly, the electric current neutralization problem has been analyzed, still for a single-aperture simulation, in order to show the capabilities of the model and discuss the neutralization physics. In this case, electrons are emitted from a downstream cathode plane and, apart from neutralizing the ion current downstream, they are observed to also travel upstream to neutralize, in charge, the ion beam. In fact, the charge neutralization appears to occur before the current neutralization and independently of the position of the cathode plane. Thirdly, a simulation featuring several apertures has been carried out to study the charge and current neutralization process in a more realistic scenario, featuring beamlets interaction and a neutralizer on one side of the thruster. While ion and charge density appear to remain quite symmetric with respect to the thruster symmetry axis, both the electric and electron current density show strong asymmetries and the electric current neutralization occurs at different downstream distances, depending on the aperture distance from the neutralizer.

A comparison between a single-aperture simulation and the multi-apertures one has shown that the symmetric reflection of macro-particles from the lateral domain boundaries permits to simulate both qualitatively and quantitatively (with very good agreements) the beamlets interaction physics. Nevertheless, the only approach to characterize well the thruster divergence angle remains that of the multi-aperture full-thruster simulation.

Finally, the obtained results have been compared with experiments, finding that the optimal perveance of the single and multi-apertures simulations is very close to the experimental one. Moreover, the values of the divergence angle for the multi-apertures case have shown non-negligible differences with respect to the experiments, but there is still room for improvement in the comparison.

Regarding future work, simulations featuring circular grid holes shall be carried out in order to be more realistic. Moreover, a larger number of apertures and a more realistic neutralizer position shall also be considered to approach real thruster configurations, thus permitting to better compare the numerical results with real ion thruster experimental data and validating the code.

Acknowledgments

This work has been supported by Project ESP2016-75887 (Spain's National Research and Development Plan - MINECO/ FEDER).

References

- ¹Kerslake, W., Goldman, R., and Nieberding, W., "SERT II - Mission, thruster performance, and in-flight thrust measurements," *Journal of Spacecraft and Rockets*, Vol. 8, No. 3, 1971, pp. 213–224.
- ²Aston, G., Kaufman, H., and Wilbur, P., "Ion beam divergence characteristics of two-grid accelerator systems," *AIAA Journal*, Vol. 16, 1978, pp. 516–524.
- ³Merino, M., Cichocki, F., and Ahedo, E., "Collisionless Plasma thruster plume expansion model," *Plasma Sources Science and Technology*, Vol. 24, No. 3, 2015, pp. 035006.
- ⁴Anderson, J., Katz, I., and Goebel, D., "Numerical Simulation of Two-Grid Ion Optics Using a 3D Code," *40th AIAA/ASME/SAE/ASEE Joint Propulsion Conference and Exhibit*, AIAA-2006-4834, 2004.
- ⁵Katz, I., Mikellides, I., Wirz, R., Anderson, J., and Goebel, D., "Ion Thruster Life Models," *41st AIAA/ASME/SAE/ASEE Joint Propulsion Conference and Exhibit*, AIAA 2005-4256, 2005.
- ⁶Nakano, M., Nakamura, K., Nakagawa, Y., D., T., Takao, Y., and Koizumi, H., "Numerical simulation of full-aperture-pair ion optics in a miniature ion thruster," *Physics of Plasma*, Vol. 25, No. 1, 2018.
- ⁷Wirz, R., Anderson, J., and Katz, I., "Time-Dependent Erosion of Ion Optics," *Journal of Propulsion and Power*, Vol. 7, No. 1, 2011.
- ⁸Kafafy, R., *Immersed Finite Element particle-in-cell simulations of ion propulsion*, Ph.D. thesis, Virginia Polytechnic Institute and State University, Blacksburg, VA, 2005.
- ⁹Binder, T., Pfeiffer, M., Fasoulas, s., and Leiter, H., "High-fidelity Particle-In-Cell simulations of ion thruster optics," *35th International Electric Propulsion Conference, Atlanta GA, USA, IEPC-2017-451*, 2017.
- ¹⁰Cichocki, F., Domínguez, A., Merino, M., and Ahedo, E., "A 3D hybrid code to study electric thruster plumes," *Space Propulsion Conference 2016*, No. paper 2016-3124968, Association Aéronautique et Astronautique de France, Rome, Italy, May 2-6, 2016.
- ¹¹Cichocki, F., Domínguez-Vázquez, A., Merino, M., and Ahedo, E., "Hybrid 3D model for the interaction of plasma thruster plumes with nearby objects," *Plasma Sources Science and Technology*, Vol. 26, No. 12, 2017, pp. 125008.
- ¹²Hockney, R. and Eastwood, J., *Computer simulation using particles*, CRC Press, Boca Ratón, FL, 1988.